# Enhancing a Many-Body Dipolar Rydberg Tweezer Array with Arbitrary Local Controls

Guillaume Bornet,[1,*] Gabriel Emperauger,[1] Cheng Chen,[1] Francisco Machado,[2,3] Sabrina Chern,[3] Lucas Leclerc,[1,4] Bastien Gély,[1] Yuki Torii Chew,[5] Daniel Barredo,[1,6] Thierry Lahaye,[1] Norman Y. Yao,[3] and Antoine Browaeys[1,†]

[1]*Université Paris-Saclay, Institut d'Optique Graduate School, CNRS, Laboratoire Charles Fabry, 91127 Palaiseau Cedex, France*

[2]*ITAMP, Harvard-Smithsonian Center for Astrophysics, Cambridge, Massachusetts 02138, USA*

[3]*Department of Physics, Harvard University, Cambridge, Massachusetts 02138, USA*

[4]*PASQAL SAS, 7 rue Léonard de Vinci - 91300 Massy, Paris, France*

[5]*Institute for Molecular Science, National Institutes of Natural Sciences, Okazaki 444-8585, Japan*

[6]*Nanomaterials and Nanotechnology Research Center (CINN-CSIC), Universidad de Oviedo (UO), Principado de Asturias, 33940 El Entrego, Spain*

(Received 16 February 2024; revised 1 May 2024; accepted 20 May 2024; published 24 June 2024)

We implement and characterize a protocol that enables arbitrary local controls in a dipolar atom array, where the degree of freedom is encoded in a pair of Rydberg states. Our approach relies on a combination of local addressing beams and global microwave fields. Using this method, we directly prepare two different types of three-atom entangled states, including a $W$ state and a state exhibiting finite chirality. We verify the nature of the underlying entanglement by performing quantum state tomography. Finally, leveraging our ability to measure multibasis, multibody observables, we explore the adiabatic preparation of low-energy states in a frustrated geometry consisting of a pair of triangular plaquettes. By using local addressing to tune the symmetry of the initial state, we demonstrate the ability to prepare correlated states distinguished only by correlations of their chirality (a fundamentally six-body observable). Our protocol is generic, allowing for rotations on arbitrary sub-groups of atoms within the array at arbitrary times during the experiment; this extends the scope of capabilities for quantum simulations of the dipolar XY model.

DOI: 10.1103/PhysRevLett.132.263601

The last decade has witnessed tremendous progress toward controllable many-body quantum systems [1–7]. This progress lies along two axes. On the digital front, programmable interactions in small and intermediate scale systems can be compiled into arbitrary unitary evolution [8–10]. On the analog front, a system's native interactions offer a scalable approach for realizing coherent many-body dynamics. This latter approach has emerged as a fruitful strategy for the quantum simulation of large-scale, strongly correlated many-body systems [11–15]. Combining the scalability of analog simulation with local controls inherent to the digital approach promises the opportunity to explore a broader landscape of quantum phenomena. In this quest for full many-body quantum control, various platforms ranging from neutral atoms [16–18] and trapped ions [19,20] to polar molecules [21,22] and superconducting circuits [23,24] have developed strategies to combine their native interactions with high-fidelity local rotations. This enhanced level of control has enabled the preparation of broader classes of initial states [25,26], the measurement of multibasis observables [27], and even mid-evolution gates [28]. These advances enabled the integration of novel quantum information protocols with quantum simulators [29–32].

Arrays of atoms coupled via Rydberg interactions have recently emerged as both promising quantum simulators [33,34] and information processors [35–38]. Combining ground-state Raman manipulations [39,40] with the ability to address individual atoms has already allowed for the demonstration of local rotations in such systems [41–43]. This is appropriate when the qubit is encoded, for example, in the hyperfine ground states of alkali atoms. However, when the qubit is encoded in a pair of Rydberg states, realizing an analogous procedure would require mapping coherently two Rydberg states on two hyperfine states, which is experimentally challenging [44]. This problem naturally arises for quantum simulations of the dipolar XY model [34,45,46], an important platform for the study of both correlated phases [34] and quantum metrology [47].

Here, we address this challenge by demonstrating a general protocol implementing nearly arbitrary local control in a dipolar Rydberg atom array. Our approach allows for the rotation of arbitrary classes of atoms and can be applied during any part of the experiment (i.e., initialization, evolution, and measurement). Our results are threefold. First, we benchmark our method by performing tomography on a three-atom $W$-state, demonstrating that it exhibits tripartite entanglement violating the Mermin-Bell

 

inequality [48]. Second, by using local rotations to add phases to this $W$ state, we demonstrate the preparation of states exhibiting finite chirality [49]. Both the measurement of this chirality, as well as the tomography of the system's density matrix, require access to multibasis, multibody observables. Finally, we extend our procedure to a frustrated six-atom system consisting of a pair of triangular plaquettes. By choosing different initial states, we adiabatically prepare states exhibiting both ferromagnetic and antiferromagnetic (six-body) connected chiral-chiral correlation functions.

Our setup [34,47,50] consists of two-dimensional arrays of $^{87}$Rb atoms trapped in optical tweezers. The atoms are arranged in groups of equilateral triangles [Fig. 1(a)]. We encode a qubit using two Rydberg states $|\uparrow\rangle = |60S_{1/2}, m_J = 1/2\rangle$ and $|\downarrow\rangle = |60P_{1/2}, m_J = -1/2\rangle$. The atoms are coupled via dipolar interactions, described by the XY Hamiltonian:

$$H_{\mathrm{XY}} = \frac{J}{2}\sum_{i<j}\frac{a^3}{r_{ij}^3}(\sigma_i^x\sigma_j^x + \sigma_i^y\sigma_j^y), \tag{1}$$

with $r_{ij}$ being the distance between atom $i$ and $j$, $a = 12.3(1)$ μm the lattice spacing, $J/h = -0.82(1)$ MHz the interaction strength, and $\sigma_i^{x,y,z}$ the Pauli matrices acting on spin $i$. A $\sim 45$ G magnetic field, perpendicular to the atomic plane, defines the quantization axis and ensures isotropic interactions. At the beginning of each experimental sequence, the atoms are excited from their ground state to $|\uparrow\rangle$ using stimulated Raman adiabatic passage. Once in the Rydberg manifold, subsequent microwave manipulations and XY interactions lead to a many-body state of interest. Finally, we read the state of the atoms by transferring the $|\uparrow\rangle$ population back to the ground state. The ground state atoms are then imaged while the atoms in $|\uparrow\rangle$ are lost (see more details in [51]).

Our protocol to perform multi-basis measurements relies on the combination of microwave pulses and local light shifts. The microwaves, tuned to the $|\uparrow\rangle - |\downarrow\rangle$ transition (at $\omega_0/(2\pi) \sim 16.7$ GHz), only allow for global rotations. To perform local rotations, we apply light shifts on specific atoms using addressing beams generated by reflecting a 1013 nm laser on a spatial-light modulator (SLM). This laser is blue-detuned with respect to the $6P_{3/2} - |\uparrow\rangle$ transition by $\Delta/(2\pi) \sim 400$ MHz, resulting in a light-shift $\delta \sim \Omega_{1013}^2/(4\Delta)$ for a Rabi frequency $\Omega_{1013}$ on an addressed atom [51]. As illustrated in Fig. 1(a), the atoms are addressed with different intensities to produce different values of light shifts, realizing the Hamiltonian $H_z = \sum_i \hbar\delta_i(1+\sigma_i^z)/2$, with $\delta_i = 0\delta$ (atoms not addressed), $1\delta$ or $2\delta$ (with $\delta \approx 2\pi \times 23$ MHz). This enables us to spectroscopically isolate three different classes of atoms (termed the $0\delta, 1\delta$ and $2\delta$ atoms), while also suppressing dipolar exchange across the atom classes. To perform local

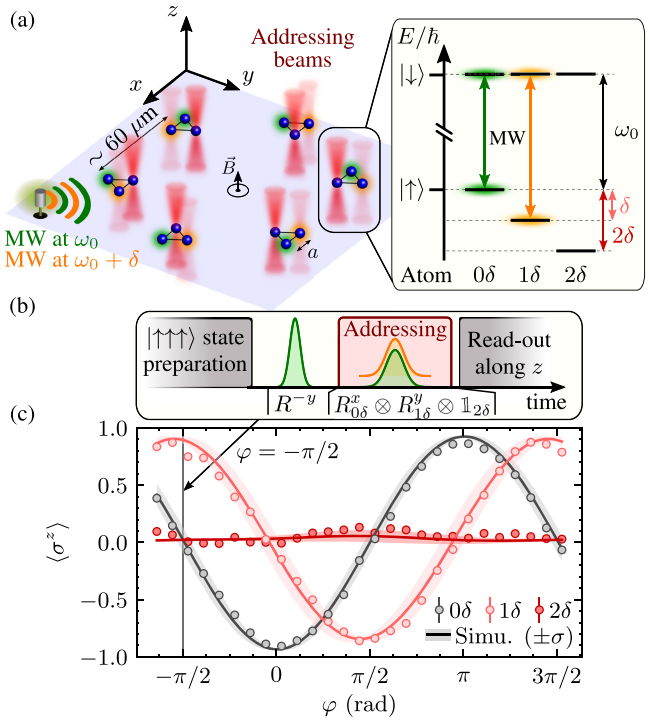


FIG. 1. Multibasis measurements protocol. (a) Experimental setup. The microwaves at a frequency $\omega_0$ ($\omega_0 + \delta$) are on resonance with the $0\delta$ ($1\delta$) atom transitions and off-resonant with the others. (b) Experimental sequence to measure the state of three atoms in the $y$, $z$, and $x$ basis. (c) Average magnetization of each class during a Ramsey experiment. The experimental sequence for $\varphi = -\pi/2$ corresponds to the one in (b). Solid lines: simulations including experimental imperfections (see text). The shaded areas represent the standard deviation.

rotations on these three classes, we apply the addressing beams and send simultaneously two microwave pulses with frequencies $\omega_0$ and $\omega_0 + \delta$, resonant with the $0\delta$ and $1\delta$ atoms [see Figs. 1(a),1(b)]. This allows for arbitrary qubit rotations of the $0\delta$ and $1\delta$ atoms while the $2\delta$ atoms remain unaffected. By applying a global rotation prior to the local ones, as detailed below, we can now perform measurements in arbitrary bases on three classes of atoms at the same time: the choice of the measurement basis is set by the duration and phase of each microwave pulse with respect to a local oscillator at $\omega_0$.

As an example, Fig. 1(b) shows the experimental sequence used to measure the $0\delta$, $1\delta$, and $2\delta$ atoms along the $y$, $z$, and $x$ axis. The first microwave pulse applies a global $\pi/2$ rotation along the $-y$. We call $R^{-y}$ the corresponding rotation operator. Then, combining two microwave frequencies with the addressing, we apply the following local rotations $R^x_{0\delta} \otimes R^y_{1\delta} \otimes \mathbb{1}_{2\delta}$ with $R^{\mathbf{u}}_{n\delta}$ the operators corresponding to a $\pi/2$ rotation of the $n\delta$ atoms around the $\mathbf{u}$ axis. This full sequence is thus equivalent to the rotations $(R^x_{0\delta}\cdot R^{-y}_{0\delta}) \otimes (R^y_{1\delta}\cdot R^{-y}_{1\delta}) \otimes R^{-y}_{2\delta}$. As, $R^x_{1\delta} \cdot R^{-y}_{1\delta} = R^z_{1\delta} \cdot R^x_{1\delta}$, and as we measure in the $z$ basis, the $z$ rotation has no effect on the measured probabilities.

The sequence thus amounts to the rotation $R^{x}_{0\delta} \otimes \mathbb{1}_{1\delta} \otimes R^{-y}_{2\delta}$ [56].

We illustrate and benchmark the protocol above by performing a Ramsey experiment: starting from all atoms in $|\uparrow\rangle$, we apply a first global rotation $R^{x\cos\varphi+y\sin\varphi}$, followed by the local rotations $R^{x}_{0\delta} \otimes R^{y}_{1\delta} \otimes \mathbb{1}_{2\delta}$ and finally read out the states for various $\varphi$. Each experimental sequence is repeated ~500 times to compute the average magnetizations. We expect oscillations of the $0\delta$ and $1\delta$-atom magnetization that are out of phase by $\pi/2$. The $2\delta$-atom magnetization should remain constant at 0. Figure 1(c) shows the experimental results. We attribute the finite contrast of the oscillations to experimental imperfections [51]. To confirm this, we perform a Monte Carlo simulation including state preparation and measurement errors, finite Rydberg lifetime, interactions between atoms, and depumping and losses induced by the addressing [51]. Taking into account all these experimentally calibrated mechanisms in the numerics yields good agreement with the data.

We now demonstrate how the local control introduced in our work enables the preparation and detection of complex, correlated states. In particular, we investigate the entangled states of three atoms placed in an equilateral triangle and interaction via $H_{\mathrm{XY}}$. In this configuration, the interaction lifts the degeneracy between $|\uparrow\uparrow\downarrow\rangle$, $|\uparrow\downarrow\uparrow\rangle$, and $|\downarrow\uparrow\uparrow\rangle$, leading to three eigenstates $|W\rangle = (|\uparrow\uparrow\downarrow\rangle + |\uparrow\downarrow\uparrow\rangle + |\downarrow\uparrow\uparrow\rangle)/\sqrt{3}$ and $|\chi^{\pm}\rangle = (|\uparrow\uparrow\downarrow\rangle + e^{\pm i(2\pi/)}|\uparrow\downarrow\uparrow\rangle + e^{\pm i(4\pi/3)}|\downarrow\uparrow\uparrow\rangle)/\sqrt{3}$ separated in frequency by $3J/\hbar$, as shown in Fig. 2(a). Despite all states exhibiting homogeneous magnetization and two-point correlation functions, they can be distinguished through their *chirality*. The chirality $\chi$ is a spin rotationally symmetric observable that breaks time reversal symmetry and is defined for three spins $i$, $j$, and $k$ by $\langle\chi_{ijk}\rangle = \langle(\boldsymbol{\sigma}_i \times \boldsymbol{\sigma}_j)\cdot\boldsymbol{\sigma}_k\rangle$, with $\boldsymbol{\sigma}_i = \sigma^x_i\boldsymbol{x} + \sigma^y_i\boldsymbol{y} + \sigma^z_i\boldsymbol{z}$ [57]. For a classical, product state $\langle\chi\rangle$ is bounded by $\pm 1$, but this limit can be overcome for entangled states: $\langle\chi^{\pm}|\chi|\chi^{\pm}\rangle$ reaches a maximal value of $\pm 2\sqrt{3}$ [51].

In order to prepare these states, we proceed as follows. Starting from all atoms in $|\uparrow\rangle$, we apply a Gaussian microwave pulse at frequency $\omega_0 + 2J/\hbar$ to drive a direct transition from $|\uparrow\uparrow\uparrow\rangle$ to $|W\rangle$. The Rabi frequency is collectively enhanced by a factor of $\sqrt{3}$, compared to the one measured for single atom Rabi oscillation experiment [see Fig. 2(b)]. These dynamics are well captured by numerical simulations that include all identified imperfections (see [51]). Finally, we turn on the addressing light for a duration $t_{\mathrm{phase}}$ to imprint a phase $0\phi$, $1\phi$, and $2\phi$ on the $0\delta$, $1\delta$, and $2\delta$ atoms, with $\phi(t_{\mathrm{phase}}) = \int_0^{t_{\mathrm{phase}}} \delta(t)\mathrm{d}t$, thus preparing $|\chi(\phi)\rangle = (|\uparrow\uparrow\downarrow\rangle + e^{i\phi}|\uparrow\downarrow\uparrow\rangle + e^{i2\phi}|\downarrow\uparrow\uparrow\rangle)/\sqrt{3}$.

To measure the chirality, we first note that it can be written as the sum of six terms corresponding to the different permutations of $\{x, y, z\}$: $\langle\chi_{0\delta,1\delta,2\delta}\rangle = \langle\sigma^x_{0\delta}\sigma^y_{1\delta}\sigma^z_{2\delta}\rangle + \langle\sigma^y_{0\delta}\sigma^z_{1\delta}\sigma^x_{2\delta}\rangle + \langle\sigma^z_{0\delta}\sigma^x_{1\delta}\sigma^y_{2\delta}\rangle - \langle\sigma^y_{0\delta}\sigma^x_{1\delta}\sigma^z_{2\delta}\rangle - \langle\sigma^x_{0\delta}\sigma^z_{1\delta}\sigma^y_{2\delta}\rangle - \langle\sigma^z_{0\delta}\sigma^y_{1\delta}\sigma^x_{2\delta}\rangle$. For each value of $\phi$, we measure each set of bases to compute the total chirality of $|\chi(\phi)\rangle$, similarly to previous work using superconducting qubits [27]. Figure 2(c) shows the results (purple circles) as a function of $\phi$, together with the theoretical expectations. The amplitude is reduced due to experimental imperfections. Simulating each step of the sequence while accounting for these imperfections [51] leads to a better agreement between theory and experiment. From a simulation of the measurement sequence (including local rotations and the readout step) assuming a perfect state preparation [blue curve in Fig. 2(c)], we find that the main limitations of the chirality measurement are the imperfections during the measurement sequence.

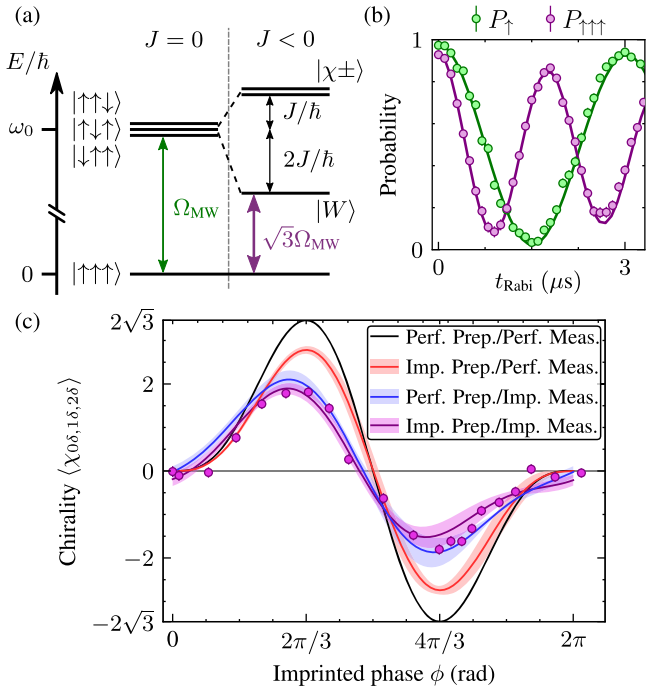


FIG. 2. $|\chi(\phi)\rangle$ state preparation. (a) Spectrum of 3 atoms in an equilateral triangle, interacting via the XY model. (b) Microwave Rabi oscillations. Green: single-atom Rabi oscillations. Purple: 3-atom Rabi oscillations with $P_{\uparrow\uparrow\uparrow}$ is the probability to measure all atoms in $|\uparrow\rangle$). Solid curves: simulations including imperfections (see text). (c) Chirality of $|\chi(\phi)\rangle$ as a function of $\phi$ (purple circles). Purple, blue, red, and black lines: Monte Carlo simulations including imperfections. The shaded areas represent the standard deviation.

We now exploit our ability to apply arbitrary local rotations to perform quantum state tomography of $|W\rangle$ and $|\chi^{\pm}\rangle$ and reconstruct their density matrix. To do so, we measure the state of each class of atoms in the $x$, $y$, and $z$ bases, corresponding to $3^3 = 27$ different measurements [51], from which we compute the relevant correlation functions, as well as extract the density matrix (using a maximum-likelihood reconstruction [51]). Figure 3 shows, for one triangle, the real and imaginary parts of the density matrices $\rho$ of the three states $|W\rangle$, $|\chi^{+}\rangle$ and $|\chi^{-}\rangle$. From

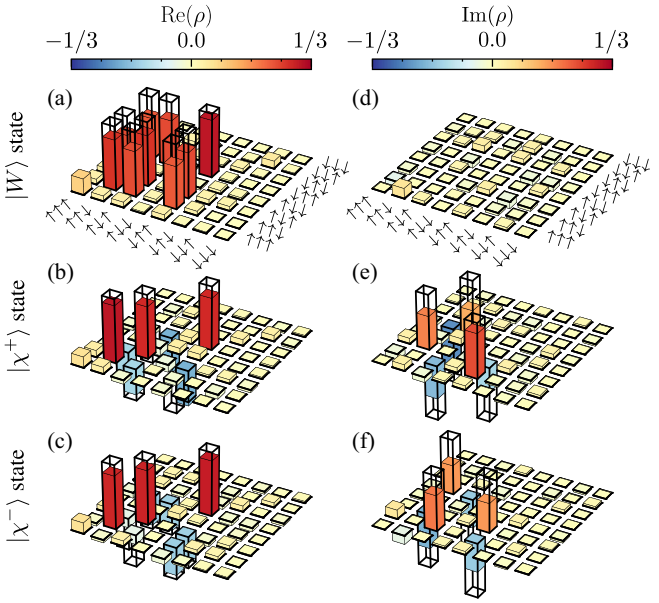


FIG. 3. State tomography. Real (a)–(c) and imaginary (d)–(f) parts of the reconstructed density matrix for the $|W\rangle$, $|\chi^+\rangle$, and $|\chi^-\rangle$ states. The transparent bars represent the expectation values for perfect states.

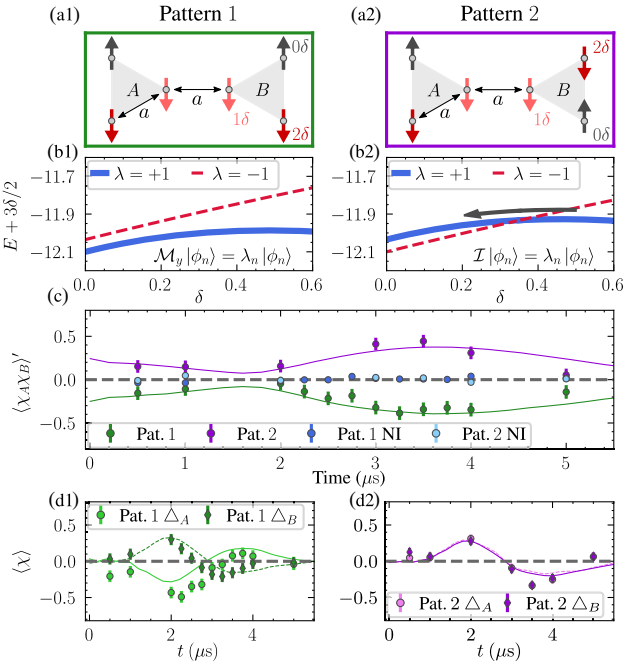


FIG. 4. Adiabatic preparation of low energy states (a) Light shift patterns $(0, 1\delta, 2\delta)$ and associated initial states. Pattern 1 respects mirror symmetry along the $y$ direction $M_y$ whereas pattern 2 respects inversion symmetry $\mathcal{I}$. (b) Energy spectrum during the adiabatic ramp for pattern 1[2]. (c) Connected chiral-chiral correlations $\langle\chi_A\chi_B\rangle'$ for pattern 1 (green), pattern 2 (purple) and noninteracting triangles (blue). The early time ($t \lesssim 1.5$ μs) observation of nonzero $\langle\chi_A\chi_B\rangle'$ is due to a necessary waiting period before measurement, during which the system undergoes additional dynamics (see [51]). (d) Chirality for triangles $A$ and $B$ under the two patterns.

them, we compute fidelities $F = \langle\psi|\rho|\psi\rangle$ of 0.74(1), 0.71(1) and 0.68(1) [0.80(1), 0.78(1), and 0.74(1) when correcting for detection errors]. They are all above 2/3, revealing genuine three-partite entanglement [58–60]. In addition, the produced $W$ state violates the Mermin-Bell inequality: $S = |\langle\sigma^z_{0\delta}\sigma^z_{1\delta}\sigma^z_{2\delta}\rangle - \langle\sigma^x_{0\delta}\sigma^x_{1\delta}\sigma^z_{2\delta}\rangle - \langle\sigma^z_{0\delta}\sigma^x_{1\delta}\sigma^z_{2\delta}\rangle - \langle\sigma^z_{0\delta}\sigma^z_{1\delta}\sigma^x_{2\delta}\rangle| \leq 2$ as we measure $S_{\text{exp}} = 2.083(26)$ [48]. Much like in the more conventional Bell-state case, this violation rules out a hidden-variable model for the measured correlations.

Having leveraged our local control to prepare and probe entangled states, we now demonstrate the power of this toolset in a quantum simulation experiment. Using a frustrated geometry consisting of a pair of triangular plaquettes [Fig. 4(a1)], we attempt to adiabatically prepare low-energy states of the antiferromagnetic dipolar XY model [61]. Owing to time-reversal symmetry, all states in the spectrum exhibit zero chirality, $\langle\chi\rangle = 0$. However, exact diagonalization demonstrates that the two lowest-energy states exhibit large, but opposite, connected chiral-chiral correlations. To illustrate this feature, we prepare both the ground and first excited states by carefully choosing an appropriate pattern of local light shifts.

Our protocol proceeds as follows [34]: after initializing all the atoms in $|\downarrow\rangle$, we turn on a pattern of local light shifts [Fig. 4(a)]; we then apply a microwave pulse to rotate the nonaddressed atoms to $|\uparrow\rangle$. This prepares a product state which is the lowest energy state of $H_z$. Starting with $\delta \gg |J|$, we then reduce the light shift as $\delta(t) = \delta_0 e^{-t/\tau}$ [with $\tau = 0.55$ μs and $\delta_0/2\pi = 23$ MHz (46 MHz) for the $1\delta(2\delta)$-atoms], thus quasi-adiabatically connecting the initial Hamiltonian ($\approx H_z$) to the final one $H_{\text{XY}}$.

In general, such an adiabatic protocol is expected to prepare the ground state of the final Hamiltonian, regardless of the details of the ramp. This expectation fails when the system's ground state exhibits a level crossing, which requires either fine-tuning or some underlying symmetry. Utilizing our ability to shape the addressing light, we thus consider two different patterns exhibiting distinct symmetries: pattern 1 respects a mirror symmetry $M_y$ along the $y$ axis [Fig. 4(a1)], while pattern 2 respects inversion symmetry $\mathcal{I}$ [Fig. 4(a2)]. For the first pattern, both initial and ground states live in the same symmetry sector of $M_y$ and thus are adiabatically connected [Fig. 4(b1)]. We thus expect to prepare the ground state, leading to the observation of *antiferromagnetic* chiral-chiral correlations. By contrast, for the second pattern, the initial and ground states live in *different* symmetry sectors of $\mathcal{I}$ and thus cannot be adiabatically connected [Fig. 4(b2)]. We thus expect to prepare the first excited state, which exhibits *ferromagnetic* chiral-chiral correlations.

We experimentally explore this difference using the multibasis measurement protocol described above. It not

only allows measuring the chirality $\langle\chi(t)\rangle$ of a single triangle, but it also enables the measurement of six-body correlation functions, from which the two-triangle connected chiral-chiral correlations, $\langle\chi_A\chi_B\rangle$, can be extracted. In principle, the full reconstruction of $\langle\chi_A\chi_B\rangle$ requires the measurement of 36 different terms. However, a smaller subset of six terms is sufficient to faithfully capture the system's correlations [51]. We can, therefore, use the same addressing pattern (and thus only a single SLM [51]) for both the adiabatic ramp and the multibasis measurement. More specifically, we measure

$$\langle\chi_A\chi_B\rangle' = \eta \sum_{a,b,c\in \mathrm{perm}(x,y,z)} \begin{matrix}\langle\sigma^a_{0\delta}\sigma^b_{1\delta}\sigma^c_{2\delta}\tilde{\sigma}^a_{0\delta}\tilde{\sigma}^b_{1\delta}\tilde{\sigma}^c_{2\delta}\rangle \\ -\langle\sigma^a_{0\delta}\sigma^b_{1\delta}\sigma^c_{2\delta}\rangle\langle\tilde{\sigma}^a_{0\delta}\tilde{\sigma}^b_{1\delta}\tilde{\sigma}^c_{2\delta}\rangle,\end{matrix} \tag{2}$$

where $\sigma[\tilde{\sigma}]$ refers to spins in triangle A[B] and $\eta = \pm 1$ is set by the relative handedness of the two three-spin measurement patterns: $\eta = -1$ for pattern 1 and $\eta = 1$ for pattern 2 [51].

We begin by studying the quasi-adiabatic ramp using the pattern depicted in Fig. 4(a1). Focusing on the connected chiral-chiral correlation, we observe the development of strong *antiferromagnetic* $\langle\chi_A\chi_B\rangle'$ correlations that persist to late times [Fig. 4(c), green]. This observation is consistent with a preparation yielding more than 50% population in the ground state [51]. By contrast, when considering the second pattern [Fig. 4(a2)], the dynamics exhibit similar features but with *opposite* sign. The presence of equally strong *ferromagnetic* $\langle\chi_A\chi_B\rangle'$ correlations is consistent with an equally large population in the first excited state of the system. To demonstrate that our observations indeed arise from the dipolar interactions between the two triangles, we also measure $\langle\chi_A\chi_B\rangle'$ for noninteracting triangles separated by $\approx 72$ μm. In this case, neither patterns lead to significant correlations [Fig. 4(c), blue].

Finally, we discuss two important sources of imperfections in our protocol. First, although $\tau$ was chosen to be much longer than the timescale of the system $(1/J)$, residual diabatic errors manifest themselves in a small chirality value $\langle\chi(t)\rangle$ [Fig. 4(d)]. Second, there are fluctuations in the positions of the atoms owing to their initial position and velocity uncertainty upon the release from the tweezers. As a result, for each repetition of the experiment, the atoms experience slightly different time-dependent interactions, that ultimately lead to the damping of the chirality oscillation and to the decay of the connected chiral-chiral correlations [51].

In conclusion, we have demonstrated a new tool combining global microwaves and local light shifts to enable local control of qubits encoded in Rydberg levels. Our protocol is generic and can be extended to an arbitrary number of classes of atoms. The agreement between experiments and simulations highlights our good understanding of error in our system—a crucial ingredient for further improvements.

More broadly, this work opens the doors to a number of intriguing directions. First, the measurement of multibody correlation functions can capture the intricate correlations that characterize complex phases of matter such as time reversal symmetry breaking and topological order [49]. Second, the ability to measure along arbitrary bases enables the implementation of novel certification protocols [62]. Finally, by interspersing unitary rotations with analog quantum simulation, one can study multitime correlation functions as well as more varied dynamical protocols [27,63–67].

This work is supported by the Agence Nationale de la Recherche (ANR-22-PETQ-0004 France 2030, project QuBitAF), and the European Research Council (Advanced Grant No. 101018511-ATARAXIA), and the Horizon Europe programme HORIZON-CL4-2022-QUANTUM-02-SGA (Project No. 101113690 PASQuanS2.1), and the U.S. Army Research Office (W911NF-21-1-0262), and the AFOSR MURI program (W911NF-20-1-0136). D. B. acknowledges support from MCIN/AEI/10.13039/501100011033 (RYC2018-025348-I, PID2020-119667GA-I00, and European Union NextGenerationEU PRTR-C17.I1). F. M. acknowledges support from the NSF through a grant for ITAMP at Harvard University. S. C. acknowledges support from the National Science Foundation Graduate Research Fellowship under Grant No. DGE 2140743.

*Corresponding author: guillaume.bornet@institutoptique.fr
†Corresponding author: antoine.browaeys@institutoptique.fr

[1] J. M. Raimond, M. Brune, and S. Haroche, Rev. Mod. Phys. **73**, 565 (2001).
[2] D. Leibfried, R. Blatt, C. Monroe, and D. Wineland, Rev. Mod. Phys. **75**, 281 (2003).
[3] H. Ritsch, P. Domokos, F. Brennecke, and T. Esslinger, Rev. Mod. Phys. **85**, 553 (2013).
[4] C. Gross and I. Bloch, Science **357**, 995 (2017).
[5] F. Schäfer, T. Fukuhara, S. Sugawa, Y. Takasu, and Y. Takahashi, Nat. Rev. Phys. **2**, 411 (2020).
[6] A. J. Heinrich, W. D. Oliver, L. M. K. Vandersypen, A. Ardavan, R. Sessoli, D. Loss, A. B. Jayich, J. Fernandez-Rossier, A. Laucht, and A. Morello, Nat. Nanotechnol. **16**, 1318 (2021).
[7] A. J. Daley, I. Bloch, C. Kokail, S. Flannigan, N. Pearson, M. Troyer, and P. Zoller, Nature (London) **607**, 667 (2022).
[8] F. Arute *et al.*, Nature (London) **574**, 505 (2019).
[9] M. Iqbal *et al.*, Nature (London) **626**, 505 (2024).
[10] D. Bluvstein *et al.*, Nature (London) **626**, 58 (2024).
[11] I. Bloch, J. Dalibard, and W. Zwerger, Rev. Mod. Phys. **80**, 885 (2008).
[12] R. Islam, R. Ma, P. M. Preiss, M. E. Tai, A. Lukin, M. Rispoli, and M. Greiner, Nature (London) **528**, 77 (2015).
[13] H. Bernien, S. Schwartz, A. Keesling, H. Levine, A. Omran, H. Pichler, S. Choi, A. S. Zibrov, M. Endres, M. Greiner, V. Vuletić, and M. D. Lukin, Nature (London) **551**, 579 (2017).
[14] S. de Léséleuc, V. Lienhard, P. Scholl, D. Barredo, S. Weber, N. Lang, H. P. Büchler, T. Lahaye, and A. Browaeys, Science **365**, 775 (2019).

[15] P. Scholl, M. Schuler, H. J. Williams, A. A. Eberharter, D. Barredo, K.-N. Schymik, V. Lienhard, L.-P. Henry, T. C. Lang, T. Lahaye, A. M. Läuchli, and A. Browaeys, Nature (London) **595**, 233 (2021).
[16] I. Bloch, J. Dalibard, and S. Nascimbène, Nat. Phys. **8**, 267 (2012).
[17] C. Gross and I. Bloch, Science **357**, 995 (2017).
[18] A. Impertro, S. Karch, J. F. Wienand, S. Huh, C. Schweizer, I. Bloch, and M. Aidelsburger, arXiv:2312.13268.
[19] R. Blatt and C. F. Roos, Nat. Phys. **8**, 277 (2012).
[20] C. Monroe, W. C. Campbell, L.-M. Duan, Z.-X. Gong, A. V. Gorshkov, P. W. Hess, R. Islam, K. Kim, N. M. Linke, G. Pagano, P. Richerme, C. Senko, and N. Y. Yao, Rev. Mod. Phys. **93**, 025001 (2021).
[21] Y. L. Zhou, M. Ortner, and P. Rabl, Phys. Rev. A **84**, 052332 (2011).
[22] B. Yan, S. A. Moses, B. Gadway, J. P. Covey, K. R. A. Hazzard, A. M. Rey, D. S. Jin, and J. Ye, Nature (London) **501**, 521 (2013).
[23] A. A. Houck, H. E. Türeci, and J. Koch, Nat. Phys. **8**, 292 (2012).
[24] M. Kjaergaard, M. E. Schwartz, J. Braumüller, P. Krantz, J. I.-J. Wang, S. Gustavsson, and W. D. Oliver, Annu. Rev. Condens. Matter Phys. **11**, 369 (2020).
[25] T. Fukuhara, P. Schauß, M. Endres, S. Hild, M. Cheneau, I. Bloch, and C. Gross, Nature (London) **502**, 76 (2013).
[26] P. T. Dumitrescu, J. G. Bohnet, J. P. Gaebler, A. Hankin, D. Hayes, A. Kumar, B. Neyenhuis, R. Vasseur, and A. C. Potter, Nature (London) **607**, 463 (2022).
[27] P. Roushan *et al.*, Nat. Phys. **13**, 146 (2017).
[28] J. Zhang, P. W. Hess, A. Kyprianidis, P. Becker, A. Lee, J. Smith, G. Pagano, I.-D. Potirniche, A. C. Potter, A. Vishwanath, N. Y. Yao, and C. Monroe, Nature (London) **543**, 217 (2017).
[29] E. Knill, D. Leibfried, R. Reichle, J. Britton, R. B. Blakestad, J. D. Jost, C. Langer, R. Ozeri, S. Seidelin, and D. J. Wineland, Phys. Rev. A **77**, 012307 (2008).
[30] J. M. Gambetta, A. D. Córcoles, S. T. Merkel, B. R. Johnson, J. A. Smolin, J. M. Chow, C. A. Ryan, C. Rigetti, S. Poletto, T. A. Ohki, M. B. Ketchen, and M. Steffen, Phys. Rev. Lett. **109**, 240504 (2012).
[31] J. P. Gaebler, A. M. Meier, T. R. Tan, R. Bowler, Y. Lin, D. Hanneke, J. D. Jost, J. P. Home, E. Knill, D. Leibfried, and D. J. Wineland, Phys. Rev. Lett. **108**, 260503 (2012).
[32] G. Pagano, A. Bapat, P. Becker, K. S. Collins, A. De, P. W. Hess, H. B. Kaplan, A. Kyprianidis, W. L. Tan, C. Baldwin, L. T. Brady, A. Deshpande, F. Liu, S. Jordan, A. V. Gorshkov, and C. Monroe, Proc. Natl. Acad. Sci. U.S.A. **117**, 25396 (2020).
[33] A. Browaeys and T. Lahaye, Nat. Phys. **16**, 132 (2020).
[34] C. Chen, G. Bornet, M. Bintz, G. Emperauger, L. Leclerc, V. S. Liu, P. Scholl, D. Barredo, J. Hauschild, S. Chatterjee, M. Schuler, A. M. Läuchli, M. P. Zaletel, T. Lahaye, N. Y. Yao, and A. Browaeys, Nature (London) **616**, 691 (2023).
[35] L. Henriet, L. Beguin, A. Signoles, T. Lahaye, A. Browaeys, G.-O. Reymond, and C. Jurczak, Quantum **4**, 327 (2020).
[36] M. Morgado and S. Whitlock, AVS Quantum Sci. **3**, 023501 (2021).
[37] T. M. Graham *et al.*, Nature (London) **604**, 457 (2022).
[38] D. Bluvstein *et al.*, Nature (London) **626**, 58 (2024).
[39] D. D. Yavuz, P. B. Kulatunga, E. Urban, T. A. Johnson, N. Proite, T. Henage, T. G. Walker, and M. Saffman, Phys. Rev. Lett. **96**, 063001 (2006).
[40] M. P. A. Jones, J. Beugnon, A. Gaëtan, J. Zhang, G. Messin, A. Browaeys, and P. Grangier, Phys. Rev. A **75**, 040301(R) (2007).
[41] L. Isenhower, E. Urban, X. L. Zhang, A. T. Gill, T. Henage, T. A. Johnson, T. G. Walker, and M. Saffman, Phys. Rev. Lett. **104**, 010503 (2010).
[42] T. Xia, M. Lichtman, K. Maller, A. W. Carr, M. J. Piotrowicz, L. Isenhower, and M. Saffman, Phys. Rev. Lett. **114**, 100503 (2015).
[43] G. Birkl and J. Fortágh, Laser Photonics Rev. **1**, 12 (2007).
[44] A. W. Glaetzle, M. Dalmonte, R. Nath, C. Gross, I. Bloch, and P. Zoller, Phys. Rev. Lett. **114**, 173002 (2015).
[45] S. Whitlock, A. W. Glaetzle, and P. Hannaford, J. Phys. B **50**, 074001 (2017).
[46] S. de Léséleuc, D. Barredo, V. Lienhard, A. Browaeys, and T. Lahaye, Phys. Rev. Lett. **119**, 053202 (2017).
[47] G. Bornet, G. Emperauger, C. Chen, B. Ye, M. Block, M. Bintz, J. A. Boyd, D. Barredo, T. Comparin, F. Mezzacapo, T. Roscilde, T. Lahaye, N. Y. Yao, and A. Browaeys, Nature (London) **621**, 728 (2023).
[48] N. D. Mermin, Phys. Rev. Lett. **65**, 1838 (1990).
[49] X. G. Wen, F. Wilczek, and A. Zee, Phys. Rev. B **39**, 11413 (1989).
[50] C. Chen, G. Emperauger, G. Bornet, F. Caleca, B. Gély, M. Bintz, S. Chatterjee, V. Liu, D. Barredo, N. Y. Yao, T. Lahaye, F. Mezzacapo, T. Roscilde, and A. Browaeys, arXiv:2311.11726.
[51] See Supplemental Material at http://link.aps.org/supplemental/10.1103/PhysRevLett.132.263601 which includes Refs. [52–55], for more details about the experimental parameters (including an analysis of the experimental imperfections) and about the numerical methods.
[52] F. Nogrette, H. Labuhn, S. Ravets, D. Barredo, L. Béguin, A. Vernier, T. Lahaye, and A. Browaeys, Phys. Rev. X **4**, 021034 (2014).
[53] D. Barredo, S. de Léséleuc, V. Lienhard, T. Lahaye, and A. Browaeys, Science **354**, 1021 (2016).
[54] I. I. Beterov, I. I. Ryabtsev, D. B. Tretyakov, and V. M. Entin, Phys. Rev. A **79**, 052504 (2009).
[55] K. Takeda, A. Noiri, T. Nakajima, J. Yoneda, T. Kobayashi, and S. Tarucha, Nat. Nanotechnol. **16**, 965 (2021).
[56] Another, more natural, experimental protocol would have been to apply 3 microwave frequencies tuned on the $0\delta$, $1\delta$, and $2\delta$ atoms. However residual spatial inhomogeneities on the $2\delta$ light shifts degraded the fidelities of the rotation in an early attempt.
[57] D. I. Tsomokos, J. J. García-Ripoll, N. R. Cooper, and J. K. Pachos, Phys. Rev. A **77**, 012106 (2008).
[58] A. Acín, D. Bruß, M. Lewenstein, and A. Sanpera, Phys. Rev. Lett. **87**, 040401 (2001).
[59] O. Gühne, P. Hyllus, D. Bruss, A. Ekert, M. Lewenstein, C. Macchiavello, and A. Sanpera, J. Mod. Opt. **50**, 1079 (2003).
[60] M. Neeley, R. C. Bialczak, M. Lenander, E. Lucero, M. Mariantoni, A. D. O'Connell, D. Sank, H. Wang, M. Weides, J. Wenner, Y. Yin, T. Yamamoto, A. N. Cleland, and J. M. Martinis, Nature (London) **467**, 570 (2010).

[61] Strictly speaking, since in Eq. (1) we have ferromagnetic couplings $J < 0$, we explore the low-energy properties of the antiferromagnetic model ($J > 0$) by preparing the highest-energy state(s) of our quasi-isolated system.
[62] S. Notarnicola, A. Elben, T. Lahaye, A. Browaeys, S. Montangero, and B. Vermersch, New J. Phys. **25**, 103006 (2023).
[63] C. Kokail, C. Maier, R. van Bijnen, T. Brydges, M. K. Joshi, P. Jurcevic, C. A. Muschik, P. Silvi, R. Blatt, C. F. Roos, and P. Zoller, Nature (London) **569**, 355 (2019).
[64] T. Brydges, A. Elben, P. Jurcevic, B. Vermersch, C. Maier, B. P. Lanyon, P. Zoller, R. Blatt, and C. F. Roos, Science **364**, 260 (2019).
[65] F. Perciavalle, D. Rossini, T. Haug, O. Morsch, and L. Amico, Phys. Rev. A **108**, 023305 (2023).
[66] L. Versini, K. A. El-Din, F. Mintert, and R. Mukherjee, arXiv:2305.01465.
[67] K. Goswami, R. Mukherjee, H. Ott, and P. Schmelcher, Phys. Rev. Res. **6**, 023031 (2024).